Bubble growth after release from an electrode

A validated CFD model

Venkatesh, N. Kodur; Krikke, I.R.C.; Valle, N.; Haverkort, J. W.

DOI
10.1016/j.electacta.2025.147827

Publication date
2026

Document Version
Final published version

Published in
Electrochimica Acta

Electrochimica Acta 547 (2026) 147827

Contents lists available at ScienceDirect

Electrochimica Acta

journal homepage: www.journals.elsevier.com/electrochimica-acta

Bubble growth after release from an electrode: A validated CFD model

N. Kodur Venkatesh *, I.R.C. Krikke, N. Valle, J.W. Haverkort

Delft University of Technology, Process & Energy Department, Leeghwaterstraat 39, 2628 CB Delft, The Netherlands

ARTICLE INFO

Keywords:
Bubble growth
Gas crossover
Dissolved gas
Alkaline water electrolysis

ABSTRACT

In water electrolysers, gas crossover caused by elevated dissolved gas concentrations poses a major challenge, reducing product purity, safety, and operational stability. However, most existing electrolyser models assume that all generated products leave the electrode in the gaseous phase, neglecting the dynamics of dissolved gas transport. Experimental observations from the literature reveal that bubbles can continue to grow even after detachment, suggesting significant dissolved gas supersaturation. In this work, we develop a computational multiphase flow model that couples the transport of dissolved gas, gas fraction, and volumetric interfacial area to quantify bubble growth within electrogenerated plumes. The model is validated using experimental data extracted from literature videos, where individual bubbles are tracked to determine their size and position over time. The absolute average relative error in predicting bubble diameters is below 7%, demonstrating the model's accuracy. Results show that at a gas-evolution efficiency of 40%, detached bubbles can grow up to 1.4 times their initial diameter, corresponding to a threefold increase in volume. This confirms that the observed post-detachment bubble growth can be quantitatively explained by the uptake of dissolved gas within the plume. By incorporating this mechanism, the model enables improved prediction of dissolved gas distributions, supporting more reliable design and operation of industrial electrolysers.

1. Introduction

Water electrolysis can play a pivotal role in the energy transition by transforming renewable electricity into green hydrogen, which can be locally produced, stored, and distributed. However, currently, only a very small percentage of global hydrogen is produced by water electrolysis [1]. Instead, hydrogen is typically produced much cheaper by reforming hydrocarbons, contributing to the emissions of CO_2. To advance the energy transition, further improvements are needed in the economics of water electrolysis, essentially through increased energy efficiency and reduced equipment and process costs [2].

Currently, the two most developed technologies are Alkaline Water Electrolysis and Proton Exchange Membrane Water Electrolysis [3]. Alkaline electrolysers are usually more cost-effective because they rely less on scarce electrode materials and are proven to be reliable and durable. These alkaline electrolysers generally use porous diaphragms to separate the produced hydrogen and oxygen bubbles. The half-reactions that occur in an alkaline water electrolyser at the cathode and anode are:

$$\text{Cathode}: 2H_2O + 2e^- \rightarrow H_2 + 2OH^- \quad (1)$$

$$\text{Anode}: 2OH^- \rightarrow \frac{1}{2}O_2 + H_2O + 2e^- \quad (2)$$

Note that the products oxygen, O_2, and hydrogen H_2 are produced in dissolved form. Since gas solubility in common electrolytes is very low (< 1 mM), supersaturation [4,5] quickly leads to the formation of gas bubbles on the surface of the electrode that absorb these dissolved gases. Most of the oxygen and hydrogen thus leave a typical electrochemical cell through buoyancy in the form of gas bubbles.

The gas bubbles impact the efficiency of water electrolysis by increasing the resistance to the flow of ions through the electrolyte, increasing ohmic losses. To prevent the accumulation of bubbles at the electrode surface, generally, the gas-evolving electrodes are oriented vertically. This orientation will cause the bubbles to form a bubble layer, or a plume, along the electrode. At high current densities, the relative importance of ohmic losses increases. An approach often used to reduce the resistance due to bubbles is to put the electrodes in a 'zero-gap' configuration, i.e.: directly adjacent to the diaphragm [6–8], such that the bubble plume evolves on the outer side of the electrode-diaphragm assembly, whereas the ions cross through the membrane.

The gas bubbles also cover a part of the electrode area, inactivating the region of the electrode and thereby increasing the activation overpotential [6–9]. At low current densities, dissolved hydrogen and

* Corresponding author.
E-mail address: N.kodurvenkatesh@tudelft.nl (N.K. Venkatesh).

https://doi.org/10.1016/j.electacta.2025.147827
Received 30 July 2025; Received in revised form 17 November 2025; Accepted 17 November 2025
Available online 22 November 2025

Nomenclature

Greek letters

ε	Gas fraction [–]
γ	Surface tension of the liquid [N/m]
μ_l	Liquid dynamic viscosity [kg/ms]
μ_m	Mixture dynamic viscosity [kg/ms]
ν_l	Liquid kinematic viscosity [m^2/s]
ρ_g	Gas density [kg/m^3]
ρ_l	Liquid density [kg/m^3]
ρ_m	Mixture density [kg/m^3]

Latin letters

a	Volumetric interfacial area [1/m]
c	Dissolved species concentration [mol/m^3]
c_s	Saturation concentration [mol/m^3]
f_g	Gas evolution efficiency [–]
j	Current density [A/m^2]
k	Interphase mass transfer coefficient [m/s]
$\mathbf{K}$	Mixture viscous stress tensor [Pa]
$\mathbf{K_l}$	Liquid viscous stress tensor [Pa]
$\hat{\mathbf{n}}$	Unit normal to the surface [–]
n	Electrons used per oxygen molecule [mol]
n_d	Bubble number density [$1/m^3$]
N_c	Dissolved species flux magnitude at the electrode [mol/m^2s]
N_d	Number density flux at electrode [$1/m^2s$]
N_g	Gas flux at electrode [m/s]
p	Pressure [Pa]
p_0	Atmospheric pressure [Pa]
$\overline{R}_{\mathrm{exp},i}$	Non-dimensional bubble radius at experimental data point i [m]
R	Bubble radius [m]
R_in	Bubble release radius at the inlet [m]
$\overline{R}_{\mathrm{sim},i}$	Non-dimensional bubble radius at simulation data point i [m]
R_out	Bubble radius at the outlet [m]
T_0	Ambient temperature [K]
$\mathbf{U}$	Volume-averaged mixture velocity [m/s]
$\mathbf{u}$	Mass-averaged mixture velocity [m/s]
$\mathbf{u_g}$	Gas velocity [m/s]
$\mathbf{u_{Hd}}$	Hydrodynamic dispersion slip velocity [m/s]
$\mathbf{u_l}$	Liquid velocity [m/s]
$\mathbf{u_s}$	Slip velocity [m/s]
$\mathbf{u_{St}}$	Stokes rise velocity [m/s]
$\dot{V}$	Volumetric interphase mass transfer rate [1/s]
$\mathcal{V}_\mathrm{m}$	Molar volume [m^3/mol]
w_st	Stokes terminal velocity [m/s]

Constants

D	Diffusion coefficient [m^2/s]
F	Faraday's constant [C/mol]
g	Acceleration due to gravity [m/s^2]
H	Henry's constant [mol/m^3Pa]
R_g	Universal gas constant [J/mol K]

oxygen reaction products can introduce a concentration overpotential [8,10]. Increasing the mass transport of dissolved gas from the electrode to the electrolyte bulk or bubbles can decrease this concentration overpotential and increase the energy efficiency.

Mass transport near gas-evolving electrodes is primarily due to a combination of micro-mixing induced by bubble motion and advective transport due to electrolyte flow [11]. These flows may be due to forced flow, but the natural convection due to rising gas bubbles can give rise to substantially large flow velocities as well [12]. The gas distribution should be accurately known to analytically model these flows and their effect on mass transport [13] and gas bubble resistance. This gas distribution is strongly influenced by the size of the bubbles through their slip velocities. While most simulations in the literature [9,14,15] use a mono-dispersed bubble size distribution, a wide range of different bubble sizes usually co-exist in experiments [9,16,17]. The size distribution of the release bubbles may still change significantly by taking up dissolved gas. Four major phenomena that affect the size of rising bubbles [9,16,18] are:

(1) Bubble coalescence
(2) Change in hydrostatic pressure
(3) Uptake of water vapour
(4) Uptake of dissolved gas

In concentrated electrolytes, coalescence (1) is strongly inhibited [19,20], and it primarily occurs close to the electrode surface or where streamlines converge [9,21]. Therefore, coalescence can usually be conveniently neglected in numerical simulations of rising bubbles in electrolytes.

The decrease in hydrostatic pressure (2) exerted on the bubbles during their ascent is insignificant unless the cell's height exceeds several meters or operates at sub-atmospheric pressure.

The presence of water vapour (3) *can* increase the size of the bubbles significantly [22]. However, this is only relevant at elevated temperatures near the boiling point of water.

In this paper, we investigate the final scenario (4), in which the diameter increases due to the addition of dissolved gas.

A fraction of the electrochemically produced dissolved gas is absorbed by the bubbles adhering to the electrode surface, which defines the so-called adherence region, and the remainder leaves the adherence region in dissolved form. From this, the gas evolution efficiency can be defined as the ratio of gas absorbed in the adherence region over the total products produced electrochemically, which is often below unity [23–27]. Note that the dissolved products released into the electrolyte can still be absorbed by rising bubbles, outside the adherence region, if the local concentration of dissolved gas is above solubility.

Usually, in multiphase flow simulations, the gas evolution efficiency is assumed to be 100%, and the interaction between dissolved gas and bubbles is not taken into account [9,14,15,28–31]. However, there are many experimental observations [9,32–34] in the literature of the growth of rising bubbles due to the uptake of dissolved gas after leaving the electrode. While these observations most often come from wire electrodes [32–34], in this study, we use the data from the videos provided in Ref. [9] for parallel plate electrodes to evaluate the performance of our model.

The interaction of the dissolved gas with bubbles *is* often taken into account in the case of interface-resolved single bubble simulations [35–41]. Including bubble growth in a volume of fluid-like model, while common in boiling simulations, has only recently been applied in electrolysis by combining it with the Euler-Euler model and including the interaction with dissolved gas [42]. There have been sparingly few studies in electrolysis that model the growth of released bubbles. An example is the Ref. [43], where authors assumed that bubbles nucleate inside the porous electrodes only above an artificially high supersaturation, giving unrealistic results. Ref. [44] provides preliminary, highly idealised simulations in Poiseuille flow. Arguably, a more relevant

example is Ref. [45], where the interaction between dissolved gas and gas volume fraction is simulated near a microwire array electrode and a vertical planar electrode. However, this model does not self-consistently include the growth in the bubble radius by coupling the transport of dissolved gas with the gas fractions, as done in our present study.

The dissolved hydrogen that is not taken up by the hydrogen bubbles can potentially cross over the anode side through the porous separator [46] and reach the oxygen side, causing an explosive mixture [47,48]. A similar risk exists for dissolved oxygen. For this reason, industrial safety standards set a maximum of 2% hydrogen to oxygen ratio. In alkaline electrolysers, this phenomenon is particularly relevant at low current densities, which severely limits the operating window of electrolysers [49]. A mathematical description of the interaction between dissolved gas and bubbles is required to model this important phenomenon.

This paper models the gas bubbles that continue to grow after they are released from the electrode and demonstrates that the uptake of dissolved gas can explain this phenomenon. The main aim of our paper is to outline the appropriate modelling equations (detailed in Section 2) to study the growth of these released bubbles and the distribution of dissolved gas concentrations and gas fractions in the bulk (detailed in Section 4). The simulation results are compared with experimental data from the literature, demonstrating that the observed bubble growth can be described satisfactorily.

2. Model

The subsequent sections present, the multiphase fluid flow model detailed in Section 2.1, which is coupled to the transport of dissolved gases through an interphase mass transfer term, elaborated in Section 2.2. Section 2.3 completes the model with the prescribed boundary conditions and the values of the parameters used in this study.

2.1. Two-phase flow model

The mixture model [50], implemented in COMSOL Multiphysics v.6.2 [51], is used to describe the two-phase flow. In the mixture model, both gas and liquid are considered as a single fluid, the mixture, of variable density and viscosity, depending on the local gas fraction, ε. The mixture density ρ_m can be expressed as $\rho_m = (1-\varepsilon)\rho_l + \varepsilon\rho_g$ and, for a negligible gas density ρ_g, $\rho_m \approx (1-\varepsilon)\rho_l$, where ρ_l is the liquid density and ε is the gas fraction, the volume of gas per unit volume. With $\mathbf{u}_g$ and $\mathbf{u}_l$ being the gas and liquid velocities, respectively, the volume-averaged mixture velocity $\mathbf{U}$ and the mass-averaged mixture velocity $\mathbf{u}$ are defined as

$$\mathbf{U} \equiv \varepsilon\mathbf{u}_g + (1-\varepsilon)\mathbf{u}_l \tag{3}$$

$$\mathbf{u} \equiv \frac{\rho_g\varepsilon\mathbf{u}_g + \rho_l(1-\varepsilon)\mathbf{u}_l}{\rho_m} \tag{4}$$

2.1.1. Multiphase flow governing equations

The governing equations for the multiphase flow consist of the conservation equations for bubble number density [Eq. (5)], gas volume fraction [Eq. (6)], mass [Eq. (7)], and momentum [Eq. (8)] of the mixture, which read:

$$\nabla\cdot(n_d\mathbf{u}_g) = 0 \tag{5}$$

$$\nabla\cdot(\varepsilon\mathbf{u}_g) = \dot{V} \tag{6}$$

$$\nabla\cdot(\rho_m\mathbf{u}) = 0 \tag{7}$$

$$\nabla\cdot\left(\rho_m\mathbf{u}\mathbf{u}\right) = -\nabla p + \nabla\cdot\mathbf{K} - \rho_m\mathbf{g} \tag{8}$$

where, n_d is the bubble number density, the number of bubbles per unit volume, p the pressure, $\mathbf{K}$ the Newtonian viscous stress tensor for the mixture and $\mathbf{g}$ the acceleration due to gravity. The term $\dot{V}$ in Eq. (6) is the volumetric source for the gas fraction due to absorption of dissolved gases in the electrolyte, detailed in Section 2.2.

The bubble number density conservation is governed by Eq. (5), assuming no coalescence or breakup of the bubbles. Note that the transport of interfacial area per unit volume a [m^2/m^3] can be obtained from bubble number density n_d and gas fraction ε [50]. In the absence of bubble coalescence and breakup, we are essentially solving the same equation through a variable bubble radius R. The gas fraction can be expressed as a product of the volume of a bubble and the bubble number density, $\varepsilon = 4\pi R^3 n_d/3$, from which we calculate the bubble radius R as

$$R = \left(\frac{3\varepsilon}{4\pi n_d}\right)^{1/3} \tag{9}$$

This effective bubble radius is thus a derived quantity obtained from the gas fraction and bubble number density and not explicitly solved for. The source term for the gas fraction, the right-hand side of Eq. (6), will lead to bubble growth. We thus obtain a spatially varying bubble radius in the simulation domain.

The Newtonian viscous stress tensor $\mathbf{K}$ for the mixture is modelled in terms of the volume-averaged mixture velocity as

$$\mathbf{K} = \mu_m\left(\nabla\mathbf{U} + \nabla\mathbf{U}^T - \frac{2}{3}(\nabla\cdot\mathbf{U})\mathbf{I}\right) \tag{10}$$

with μ_m the mixture viscosity. Since in our simulations, the gas fraction is expected to be low $\varepsilon < 5$ %, given the low current density, we simply take $\mu_m \approx \mu_l$, the liquid viscosity.

2.1.2. Slip velocities

The slip velocity $\mathbf{u}_s \equiv \mathbf{u}_g - \mathbf{u}_l$ accounts for the relative motion of the gas phase with respect to the liquid and is modelled as [14,15,28]:

$$\mathbf{u}_s = \mathbf{u}_{St} + \mathbf{u}_{Hd} \tag{11}$$

where $\mathbf{u}_{St}$ is the Stokes rise velocity and $\mathbf{u}_{Hd}$ is hydrodynamic dispersion. The primary slip velocity, the Stokes rise velocity in the upward direction $\hat{\mathbf{z}}$, is given by

$$\mathbf{u}_{St} = w_{St}\hat{\mathbf{z}} \text{ where } w_{St} = \frac{2\,gR^2}{9\nu_l} \tag{12}$$

where $\nu_l = \mu_l/\rho_l$ is the liquid kinematic viscosity. The Stokes terminal velocity w_{St} results from the balance between buoyancy and viscous forces under the assumptions of creeping flow around an undeformed spherical bubble. A term that we do not include here is the hindrance factor [14,52,53], which is known to slow down settling solid particles at higher volume fractions. Since we expect relatively low gas fractions, working with low current densities, this effect can be neglected.

The second term in Eq. (11) represents the hydrodynamic dispersion [53–58], which arises as rising bubbles interact. We will use:

$$\mathbf{u}_{Hd} = -\frac{\mathbf{D}_{Hd}\cdot\nabla\varepsilon}{\varepsilon(1-\varepsilon)} \text{ where } \mathbf{D}_{Hd} = Rw_{St}\begin{bmatrix}1 & 0\\ 0 & 8\end{bmatrix} \tag{13}$$

which was found to describe the transverse settling of solid spheres well. Other effects, like the Saffmann lift [59–61], shear dispersion and shear migration [62] used in the reference studies [14,28] are excluded here as they are expected to have a negligible effect for the low gas fractions considered here. Owing to these small gas fractions, we also do not use solid pressure models that account for the long-term contact forces used in the modelling of bubbly flows with relatively high gas fractions [58].

2.2. Dissolved gas transport

As discussed in the introduction, most models reported in the literature use a gas evolution efficiency of 100%. In reality, some of the dissolved gas may leave the adherence region along with the bubble plume at the electrode surface.

The concentration of dissolved species/gas c [mol/m^3], is modelled by the advection–diffusion equation shown in Eq. (14). The volumetric source $\dot{V}$, in the right-hand side of Eq. (6), serves as the molar sink when divided by the molar volume $\mathcal{V}_m$.

$$\nabla \cdot (\mathbf{u}_l c - D\nabla c) = -\frac{\dot{V}}{\mathcal{V}_m} \tag{14}$$

where molecular diffusion is given by D and u_l is the liquid velocity obtained from solving the fluid flow equations. Thus Eq. (14), along with Eqs. (5), (6), (7) and (8), complete the governing equations of the system.

The interfacial volume transfer rate $\dot{V}$ [1/s] from the liquid to the bubbles is modelled as:

$$\dot{V} = ka\left(c - c_s\right)\mathcal{V}_m \tag{15}$$

Where $c_s = 1.3$ [mol/m^3] is the saturation concentration at the surface of the gas–liquid interface. The value of this saturation concentration is obtained from Henry's law as $c_s = H(\frac{2\gamma}{R} + p_0)$, where H is the Henry's constant, and p_0 the atmospheric pressure. Note that the Laplace pressure due to surface tension is only comparable to atmospheric pressure when the bubble radius is in the order of 1 μm. For bubbles in this study, with radii greater than 40 μm, the Laplace pressure is only 3% of the atmospheric pressure, and hence the changes in the dissolved gas concentration at the bubble surface, due to surface tension, are negligible. The interfacial surface area per unit volume a [m^2/m^3], for bubbles of uniform radius R, can be obtained from the product of the individual bubble's surface area ($4\pi R^2$) with the bubble number density (n_d), which can be reduced to,

$$a = \frac{3\epsilon}{R} = \left(36\pi\epsilon^2 n_d\right)^{1/3} \tag{16}$$

where in the final expression, we insert Eq. (9). Assuming Stokes flow, neglecting coalescence and internal circulation within the bubble, the interfacial mass transfer coefficient k, into a single sphere can be modelled reasonably accurately by [63,64]

$$k \approx \frac{D}{2R}\left(1 + \left(1 + \frac{2Ru_s}{D}\right)^{1/3}\right) \tag{17}$$

with D the molecular diffusion coefficient of the dissolved gas. For a typical $2R = 100$ μm bubble $2Ru_{St}/\nu$ is in the order of unity, but $2Ru_{St}/D \gg 1$ because $D \ll \nu$ in liquids.

As mentioned earlier, the radius of the bubbles changes according to Eq. (9) as the gas fraction ϵ and the bubble number density n_d change. Through Eqs. (6) and (15), dissolved gas is converted to gas fraction, which increases the bubble radius. We note that this change in radius, in turn, also impacts the gas distribution by changing the slip velocities $\mathbf{u}_s$ through Eqs. (11) and (13), which is accounted for in this model. An increased bubble size will lead to more dispersion and, thus, wider gas plumes.

2.3. Boundary conditions

At the electrode (see Fig. 1), a boundary condition for the gas flux N_g is imposed through

$$N_g = \frac{j f_g \mathcal{V}_m}{nF} \tag{18}$$

where j is the local current density, f_g is the gas evolution efficiency, $F \approx 96,485$ [C/mol], is the Faraday's constant and $n = 4$, the number of moles of electrons required to generate one mole of the product(oxygen). For an ideal gas at a pressure p_0, temperature T_0 and R_g as the universal gas constant, the molar volume is given as $\mathcal{V}_m = R_g T_0/p_0$.

The flux of dissolved species or dissolved gas N_c at the electrode is given by

$$N_c = \frac{j(1 - f_g)}{nF} \tag{19}$$

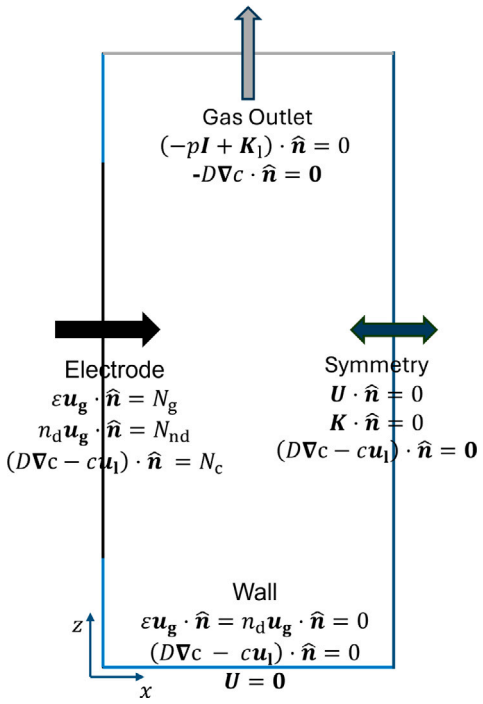

Fig. 1. This figure (not to scale) shows the boundary conditions used for the respective domains. The term $\hat{\mathbf{n}}$ represents the unit vector normal to the boundary pointing inwards. The regions above and below the electrode are non-reacting walls (shown in blue). The air–liquid interface at the top allows only the gas to leave the domain, and at the centre of the channel (shown with a double-sided arrow), a symmetry condition is used. The terms $\mathbf{K}$ and $\mathbf{K_l} = \mathbf{K} - \epsilon(1-\epsilon)(\rho_l + \rho_g - \rho_m)\mathbf{u}_s\mathbf{u}_s$ represent the mixture and liquid viscous stress tensors, respectively. The conditions for the number density flux $N_{nd} = N_g/(4\pi R^3/3)$ and concentration flux N_c are shown through Eqs. (18) and (19) respectively.

where j is the local current density, f_g is the gas evolution efficiency, F is Faraday's constant and $n = 4$ is the number of moles of electrons required to generate one mole of the product (Oxygen). The air–liquid interface at the top is modelled to have no outward normal diffusive flux, whereas the walls and symmetry are modelled with no net normal flux, as shown in Fig. 1.

At the top of the domain is the air–liquid interface, which allows only gas to escape. This is modelled by equating the normal components of the sum of the liquid viscous stress tensor and pressure to zero. To reduce computational effort, only half of the domain is simulated, with a symmetry condition at the mid-section of the channel implemented by equating the normal components of the mixture stress tensor $\mathbf{K}$ and the volume-averaged mixture velocity to zero. The walls impose a no-slip condition on the mixture velocity and a no-penetration condition for the gas fraction and number density. The respective equations for these boundaries are specified in Fig. 1.

The values of all the general parameters used in the study are outlined in Table 1.

3. Methodology

The videos from the experiments of Hreiz et al. [9] were analysed to visualise the bubble growth and trajectories of rising bubbles. The authors provide six videos, two each, for three average current density cases. The two videos include one for the upper half section of the channel and another for the lower half. It was observed that the video for the lower half of the 130 A/m^2 current density case showed considerable bubble growth and clearly recognisable bubble outlines, and hence, was chosen to obtain validation data for this study.

Table 1
The values of the different parameters used in this study. The values are taken at ambient temperature of 20 °C. The diffusion coefficient [65] and Henry's constant [65] for oxygen are considered in this study.

Parameter(Symbol)	Value (SI units)
Liquid density (ρ_l)	1005 [kg/m^3]
Gas density (ρ_g)	1.32 [kg/m^3]
Liquid viscosity (μ_l)	8.9×10^{-4} [Pa s]
Surface tension (γ)	0.072 [N/m]
Diffusion coefficient (D)	2.3×10^{-9} [m^2/s]
Henry's constant (H)	1.3×10^{-5} [mol/Pa m^3]
Faraday's constant (F)	96,485 [C/mol]
Gas constant (R_g)	8.314 [J/mol K]

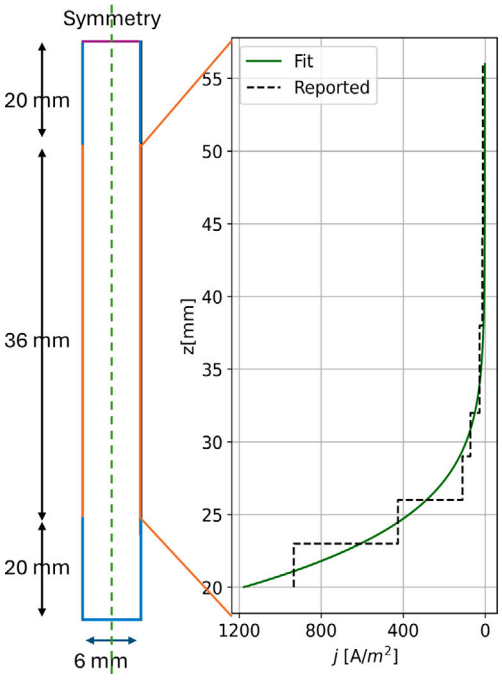

Fig. 2. (left) The dimensions of the electrode channel assembly of Hreiz et al. [9] and the simulation geometry used in this study (not to scale). (right) Reported values for the current density along with our fit $j = 0.004z^{-2} + 9219e^{-5168z^2}$ [A/m^2] with z in [m]. This continuous and differentiable function for current density is chosen for numerical stability.

The details of the electrode channel assembly are shown in Section 3.1, the methods used to obtain the validation data in Section 3.2 and the approach to obtain comparable simulation data in Section 3.3. The mesh used along with the grid convergence study is presented in Section 3.4.

3.1. Configuration and current density

The experiments of Ref. [9] were conducted in a vertical channel with oxygen evolution on both sides; see Fig. 2. The hydrogen evolution occurs on electrodes outside the channel [18]. This configuration leads to strong inhomogeneous current distributions along the electrode, see Fig. 2, with very high current densities reported at the bottom sections of the electrode and almost no reaction occurring in the top section. The reference study [9] reports different current values for six sections of the electrode and their respective dimensions with an average current density of 130 A/m^2 over the entire electrode. For numerical stability, a curve is fit to match the reported overall average current density.

3.2. Experimental data

Fourteen individual bubbles were manually tracked from the bottom section of the channel, corresponding to approximately 25 mm of the electrode. The bubble positions and their respective diameters at the corresponding position were measured using the software ImageJ [66]. An example of the bubble trajectory and the approach is shown in Fig. A.1. The two-dimensional frontal area of the bubble (in pixel^2), sampled every ten frames, is used to calculate the diameter with an accuracy of 1 px $\approx$ 20 µm. The bubble trajectories were obtained with similar accuracy by recording the coordinates of the bubbles' centre points for every frame using ImageJ software's manual tracking feature. This dataset is used to compare with the simulations for bubble diameter growth. Note that, from this method, we only get the velocity and the position of the bubble and not their release locations along the electrode. The initial x direction velocity was used to extrapolate their release locations. The diameters measured in the first frame were taken as their release diameters R_{in}. More details on the approach used to collect the diameter data are presented in Appendix A.

3.3. Particle tracking simulations

To obtain bubble growth data from simulations, we inject 72 massless tracer particles with uniform release diameters at equidistant release locations along the electrode. The released particles follow the gas velocity $\mathbf{u}_g$, obtained by solving the coupled governing equations detailed in Section 2. Note that the gas velocity obtained from the flow field includes the slip velocities mentioned in Eqs. (11)–(13). We extract particle diameters by interpolating each trajectory against the bubble-diameter distribution, obtained using Eq. (9), and then use these diameters for the comparisons in the following sections. The trajectories of the particles chosen for comparison are such that they represent the upper and lower bounds of the release heights of the bubbles traced from the experiments. More details on the particle tracing simulations are presented in Appendix B.

3.4. Mesh and implementation

To capture the concentration boundary layer, small mesh elements are needed close to the electrode. Small elements are also required at the bottom of the electrode owing to the current distribution (Fig. 2). Thus, all the meshes chosen for the grid convergence study have smaller elements closer to the electrode and larger elements in the centre of the channel. Similarly, the mesh elements from the bottom to the top of the electrode increase in size.

Three meshes (coarse, medium and fine) with a grid refinement factor [67] of $r = 2$ were chosen for the study. The mesh sensitivity was found to be much higher for number density than for dissolved gas concentration. Fig. 3 shows the average values of dissolved gas concentration and bubble number density along the electrode, based on which the grid convergence index was estimated. The number density-based grid convergence index[1] (GCI) for coarse and medium mesh is calculated to be $GCI_{12} \approx 23\%$, and that for the medium and fine mesh is calculated as $GCI_{23} \approx 12\%$. Based on this grid convergence index, the medium mesh was chosen for the subsequent simulations.

The final mesh has a smallest element size of approximately 0.01 mm close to the electrode and a largest element size of 0.05 mm, at the centre of the channel in the x-direction. In the z-direction, the final mesh has a minimum element size of 0.02 mm and a maximum element size of 0.125 mm. Overall, the chosen mesh has approximately 68,000 elements. The mesh element size distribution in the domain is shown in Fig. 4.

[1] Grid convergence index (GCI) is calculated as $GCI_{12} = \frac{|f_2 - f_1|}{f_1(r^p - 1)}$ where, $p = \frac{\ln((f_3 - f_2)/(f_2 - f_1))}{\ln(r)}$ and r is the mesh refinement factor. The asymptotic grid convergence is reached when the $GCI_{23}/GCI_{12} \approx 1$. [67]

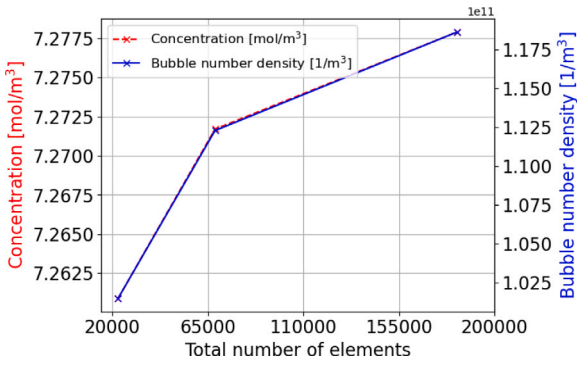

Fig. 3. The values of dissolved gas concentration (left y-axis) and the bubble number density (right y-axis), averaged along the height of the electrode, against the number of elements in the domain. The error between the fine mesh and medium mesh for number density is approximately 5.6%, and the same for concentration is 0.08%.

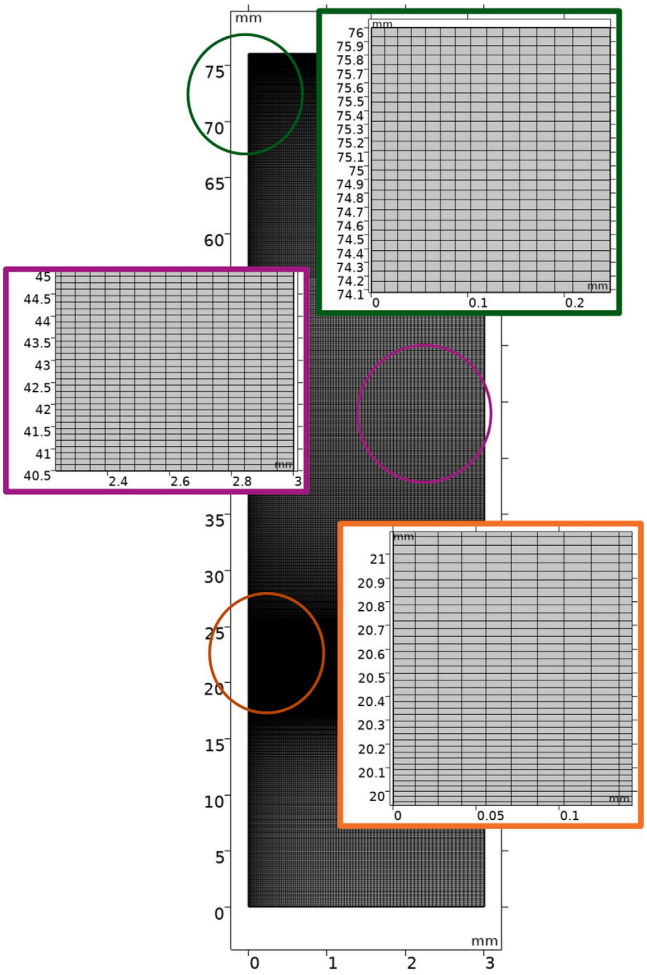

Fig. 4. The element size distribution of the mesh used in the simulations.

The governing equations were implemented in COMSOL Multiphysics v.6.2 [51]. The number density conservation Eq. (5) is implemented in terms of volume-averaged mixture velocity and slip-flux. According to the COMSOL manual [51] (page 614), the right-hand side of the equation should be proportional to $(\frac{1}{\rho_l} - \frac{1}{\rho_g})$ but was wrongly implemented as proportional to $(\frac{1}{\rho_l} + \frac{1}{\rho_g})$ leading to conservation issues. We have corrected this error in the implementation of the number density equation present in this version.

4. Results

The primary results include a comparison of the simulation with experimental data [9] outlined in Section 4.1. The effects of gas evolution efficiency and bubble release radius on the growth rates are discussed in Section 4.2.

4.1. Bubble growth

The bubble radius from the experiments [9], shown in Fig. 5(top), grows up to 40% of their release radius, almost tripling the bubble volume. This indicates that a significant fraction of the gas ends up in the bubbles during their rise. Note that the radii R of the bubbles from experiments shown in Fig. 5(top) are non-dimensionalised with their measured release diameter R_{in}. As a rough estimate, let us assume that the average bubble increases in radius by a factor $R_{out}/R_{in} \approx 1.35$, with R_{out} being the final bubble radius from the experimental data. Assuming that the released bubbles absorb all the dissolved gas, from the definition of the gas evolution efficiency, we have $f_g \approx (R_{in}/R_{out})^3 \approx 0.4$. This is the value of f_g we use in the simulations, whose resulting dissolved gas concentration is shown in Fig. 6(bottom). The bubble trajectories obtained from particle tracing, indicated by white dashed lines, are overlayed in Fig. 5(bottom). Trajectories are chosen to represent the lowest and highest release locations of the bubbles in the experiments, labelled as 'a' and 'b', respectively. The bubble diameters associated with these trajectories are shown in Fig. 5(top) with blue dashed lines. Note that the rest of the bubble trajectories are not displayed in the figure to make the presentation clearer. To see all the trajectories and their respective diameters in the simulations, see Appendix B.

The bubble radius can be seen to grow mostly near the bottom of the electrode, where the dissolved gas concentration is the largest, owing to the higher current distribution. The bubble growth stagnates when the bubble moves away from the electrodes, where the dissolved gas is lower, as seen for trajectory 'a'. The bubble in trajectory 'b' does not exhibit growth as steep as 'a' since it is released from a region of lower concentration. The experimental data (in red) also shows several bubbles with larger growth when released at the bottom compared to the ones released at the top of the electrode. The reason is evident from Fig. 5(bottom): by comparing curves 'a' and 'b', bubbles that start at lower heights, like 'a', originate from the region of high dissolved gas concentration but curve away from the electrode sooner. Whereas, the bubbles released from higher sections of the electrode, although originating from a region of lower gas concentration, have a larger residence time in the concentration boundary layer, thus exhibiting low but steady growth rates.

The sharp depletion of dissolved gas along the height of the electrode can be explained by the gas fraction distribution shown in Fig. 6(bottom) and the current density distribution shown in Fig. 2. Since the gas fraction in the bottom section of the electrode is substantially larger, the dissolved gas is absorbed by the bubbles. This, in combination with the low flux of dissolved gas along the height, leads to a significant depletion of dissolved gas. The resulting bubble diameter distribution obtained from the simulations, assuming all bubbles start with an equal diameter $R_{in} = 40$ μm, is shown in Fig. 6(top). The gas fraction distribution shows that the gas fractions everywhere stay below 5%, warranting our neglect of an effect on the mixture viscosity, hindrance and other bubble effects that only become important at higher gas fractions.

We note that in our continuum model, the particle path lines are smooth curves that do not overlap and thus are contained between the path lines 'a' and 'b'. Due to bubble–bubble interactions, actual

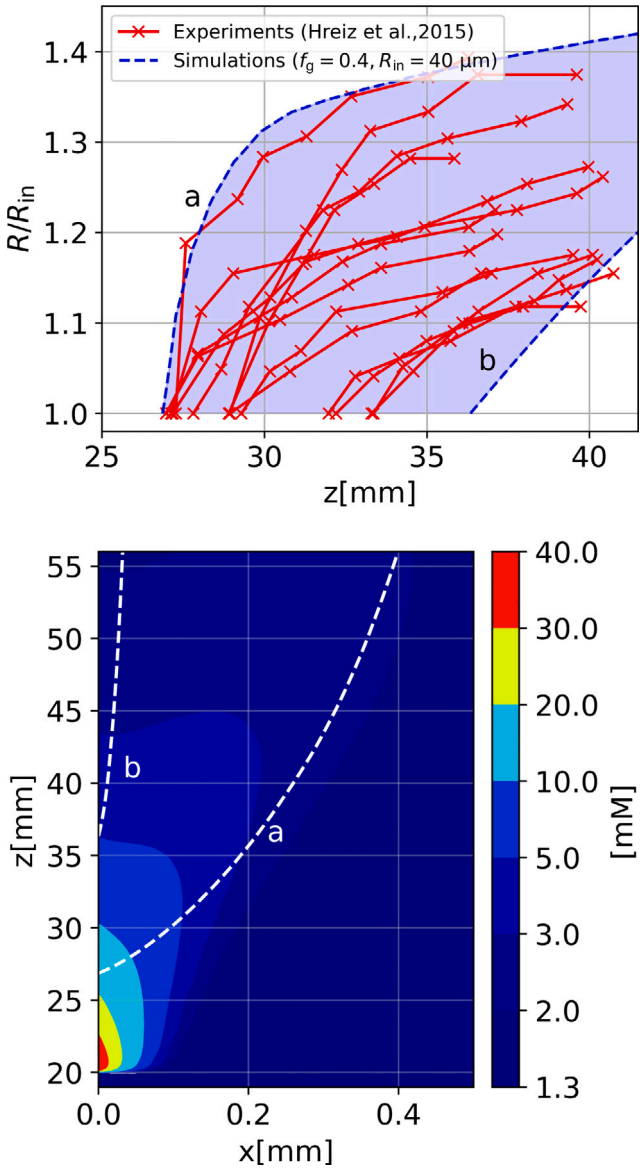

Fig. 5. (top) The non-dimensionalised bubble radii from experimental videos (see Section 3.2) compared with the simulation results (see Section 3.3) as a function of electrode height. These radii are non-dimensionalised with their release radii R_{in}. The envelopes 'a' and 'b' correspond to bubble diameters along the trajectories shown in the bottom figure that represent the minimum and maximum release heights seen in the experiment. (bottom) The bubble trajectories 'a' and 'b', overlaying the dissolved oxygen concentration contour [mol/m^3] (in colour). The dissolved gas distribution sharply drops along height due to decreasing current density (see Fig. 2) and higher gas fraction in the bottom (see Fig. 6) that absorbs this dissolved gas.

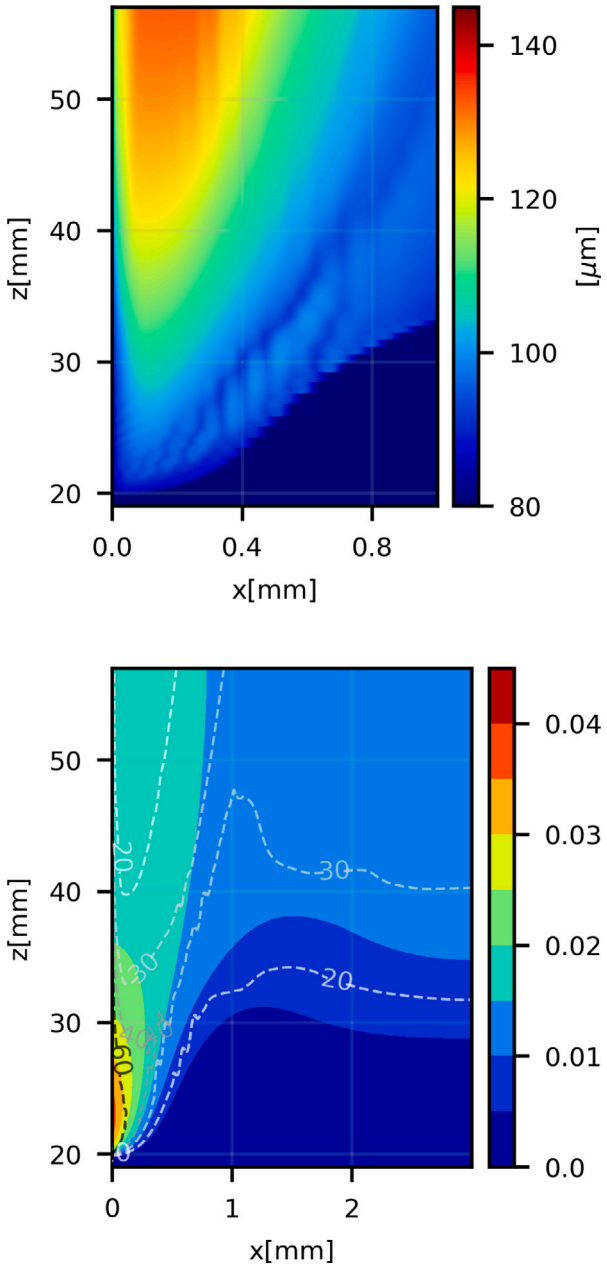

Fig. 6. (top) The diameter in [μm] obtained from the simulations of bubbles starting with $2R_{in}$ = 80 μm and a gas evolution efficiency of f_g = 40%. (bottom) The gas fraction contours (in colour) overlayed with the bubble number density in [1/mm^3] from which the bubble radius is obtained using Eq. (9).

bubbles will follow irregular trajectories that can instantaneously even move towards the electrode. The hydrodynamic dispersion coefficient of Eq. (13) describes these random motions on average seemingly quite well, resulting in good agreement between the predicted and observed curves in Fig. 5.

To quantify the error in predicting the diameter of the released bubble, we use the results of the particle tracking simulations and the particle tracking data from the experiments. The radii of the bubbles, at every measurement point along the bubble trajectories in the experiments, non-dimensionalised with the respective release radii, are compared with the non-dimensional bubble radii predicted by the simulations for the trajectories with the same release heights. With N as the number of experimental data points, the average relative error is calculated as $\frac{1}{N}\Sigma_1^N\left(\frac{\bar{R}_{exp,i}-\bar{R}_{sim,i}}{\bar{R}_{sim,i}}\right) = -5.0\%$, suggesting that the model marginally over-predicts the bubble diameter growth. The absolute average relative error is calculated as $\frac{1}{N}\Sigma_1^N\frac{|\bar{R}_{exp,i}-\bar{R}_{sim,i}|}{\bar{R}_{sim,i}} = 6.2\%$. This error includes the manual error in measuring the frontal area of the bubbles from the experimental videos and the errors arising due to difference in trajectories between experiments and simulations.

4.2. Varying gas evolution efficiency and bubble release radius

The gas evolution efficiency f_g depends on the bubble coverage, the extent of micromixing due to bubble release and mass transfer towards

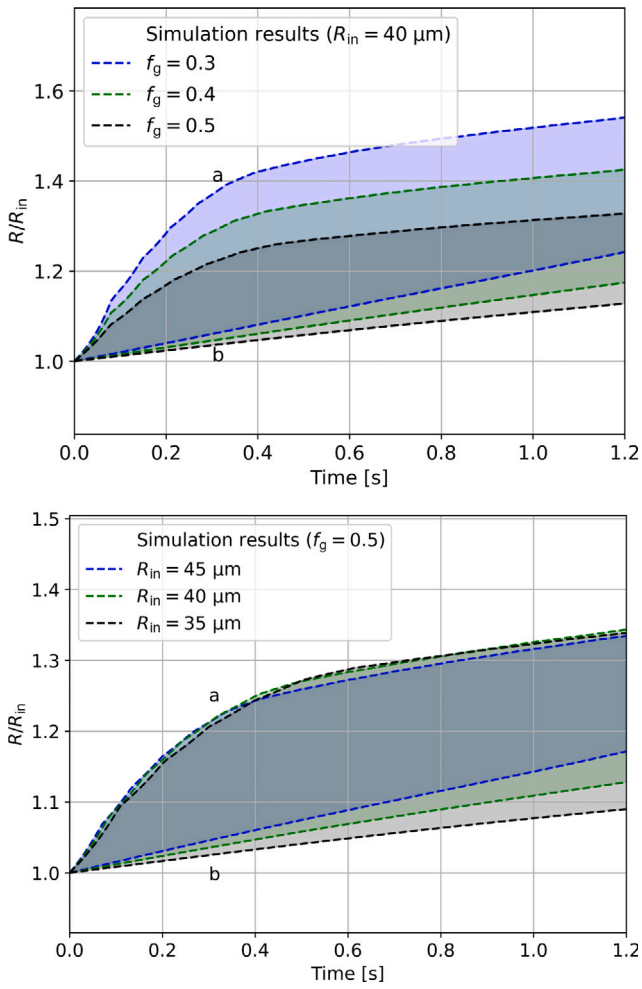

Fig. 7. (top) The bubble growth for different values of gas evolution efficiency (f_g). (bottom) The bubble growth for different inlet diameters in the simulation. 'a' and 'b' correspond to the bubble trajectories at the same release heights shown in Fig. 5. While these bubble trajectories do not change significantly by varying the inlet diameter (R_{in}), varying the gas evolution efficiency (f_g) has a noticeable impact which is reflected in their bubble growth rates.

the adhered bubbles relative to the mass transfer to the bulk, which is beyond the scope of this study. Therefore, this section investigates the sensitivity of the model to the parameter governing gas evolution efficiency f_g.

The value of $f_g = 0.4$ used in the main text is compared to values of 0.3 and 0.5 in Fig. 7(top). As the gas evolution efficiency decreases, the growth rate of the detached bubble increases, which is an expected consequence of a larger flux of dissolved gas in the electrolyte.

Fig. 7(bottom) compares the value for the detachment diameter $R_{in} = 40$ µm with values of 35 µm and 45 µm. This small variation in release diameter only results in modest changes in the x-velocities of the bubbles, subtly changing their path lines and, hence, their growth rates only marginally. An interesting observation here, is the increase in the range of bubble diameters with decreasing inlet diameter, indicating a slight increase in the polydispersity of bubble sizes.

5. Conclusion and discussion

A new numerical model has been presented and validated to predict the growth of bubbles in an electrolyser after detachment. The model highlights the importance of using a gas evolution efficiency less than unity to obtain realistic results. We show that the bubble diameter can grow significantly, and in the present case, it causes some bubbles to almost triple in volume. The absolute average relative error in predicting the bubble diameter using this model is less than 7%.

We note that the relatively large bubble growth observed in Ref. [9] may be quite different in other configurations. The relatively localised production of gas due to the inhomogeneous current distribution, combined with a low gas fraction, leads to high supersaturations of dissolved gas. At atmospheric pressures, the gas fractions are much higher at the high current densities in electrolysers typically seen in industry, and the bubble growth would not be this significant. However, at elevated pressures, the gas fractions can be much lower, and the bubbles may grow much more away from the electrode.

Our model provides a detailed picture of the dissolved gas concentration distribution and its effect on the growth rate of the bubbles. An accurate description of dissolved gas is a necessary first step to describe gas cross-over, which limits the operational window of electrolysers. As such, this is an important next step towards a more complete description of this important phenomenon.

Future work would include the validation of the model for a wider range of current densities, and to improve the agreement on the velocity field, should relevant experimental datasets become available.

CRediT authorship contribution statement

N. Kodur Venkatesh: Writing – review & editing, Writing – original draft. **I.R.C. Krikke:** Writing – original draft, Conceptualization. **N. Valle:** Writing – review & editing, Supervision. **J.W. Haverkort:** Writing – review & editing, Supervision.

Declaration of competing interest

The authors declare the following financial interests/personal relationships which may be considered as potential competing interests: J. W. Haverkort reports financial support was provided by Dutch Research Council. If there are other authors, they declare that they have no known competing financial interests or personal relationships that could have appeared to influence the work reported in this paper.

Acknowledgements

This publication is part of the project "Hydrogen bubbles quantified" (Vidi grant with project number 19665) which is (partly) financed by the Dutch Research Council (NWO).

Appendix A. Experimental data

This section provides more information on how the bubble growth data was obtained from the experiments of Hreiz et al. (2015) [9]. The video of the lower segment, corresponding to the experimental case corresponding to the current density of 130 A/m^2, was converted to a still image sequence. The bubbles chosen to represent the data were such that they were close to the electrode, and the bubble outlines were clearly visible through all the frames under consideration. The frames were analysed manually using ImageJ [66] to get coordinates of the centre of the bubble to obtain its position (x and z coordinates) in every frame to obtain the trajectory. The trajectory of one such traced bubble is shown in Fig. A.1-left.

The 2−dimensional cross-sectional area of the bubble was obtained every 10 frames by drawing a circular mask along the visible outline and measuring the masking area within the circle using the measure feature of ImageJ. One such example is shown in Fig. A.1-right. The diameter was then obtained from the 2D area. All the values were converted from pixels to millimetres using the channel width dimensions provided in the references [9,18]. The individual bubble diameters obtained in this method are plotted in Fig. A.2.

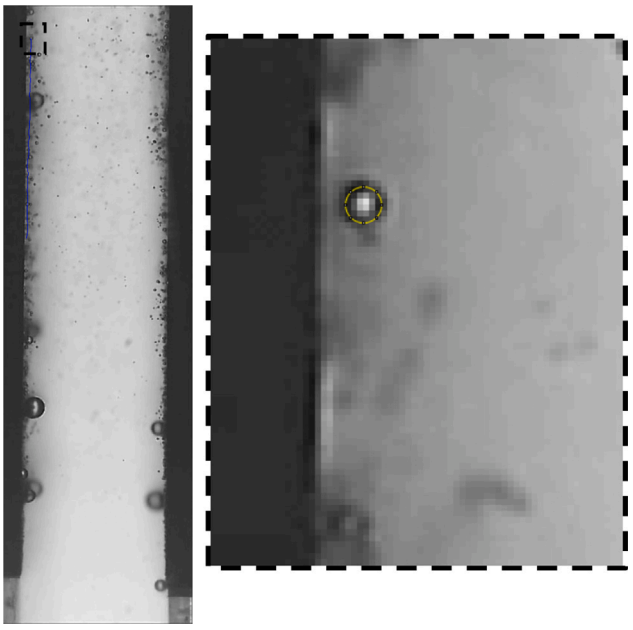

Fig. A.1. Left: The trajectory of one of the bubbles traced in blue. Right: The method used to measure the diameter of the bubble at the instant. The images were obtained from the video provided in Ref. [9] for an average current density of 130 A/m^2 and analysed using ImageJ [66].

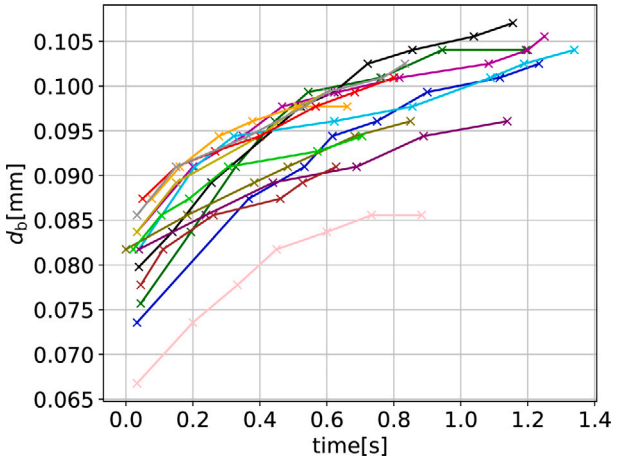

Fig. A.2. The bubble diameters (d_b) obtained through the measurement technique outlined in Appendix A. This data is used for validation in this study. It can be noted that non-dimensionalising with the release diameter is ideal for comparison with a single inlet diameter simulation.

The distribution of dissolved gas concentrations and bubble growth in the vicinity of an electrode depends on the current density distribution at the electrode. The authors in Ref. [9] provide videos for three different values of average current densities, but only one current distribution data set is presented for the case of 130 A/m^2. In their preceding works [68], they provide the current distribution for cases with different channel widths but without the corresponding videos. Thus, we are unable to extend the validation to other current densities in the present study.

Figure 4 in Ref. [9] provides a contour plot of the gas-phase velocity obtained using particle image velocimetry (PIV). However, it is difficult to extract the velocity profiles from the aforementioned contour plot. Therefore, we reproduced the results with the videos from the reference article. The gas-phase velocity obtained from the experiments

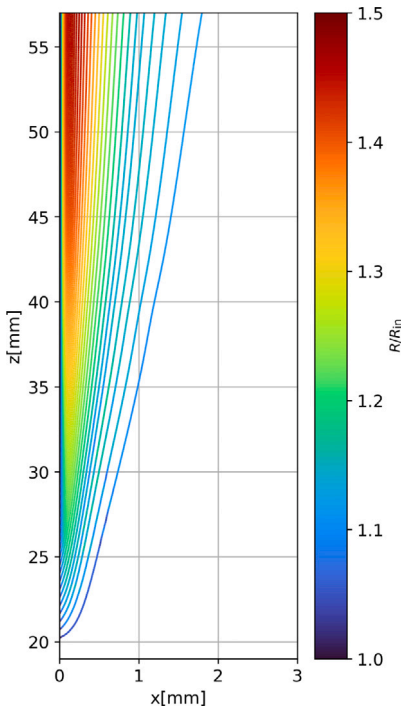

Fig. B.1. The trajectories of the particle tracing simulations, from which the diameter data is obtained, to compare with the experimental data. The trajectories are coloured by radius R and non-dimensionalised by inlet radius R_{in}.

was asymmetric, with approximately 14% higher velocity on the right electrode, despite being in a symmetric setup and both electrodes evolving oxygen. Furthermore, the large bubbles adhering to the electrode's surface distorted the local flow field around the bubble, further complicating a comparison with our simulations. Despite these issues, the gas-phase velocity field obtained from the present model matches that obtained from the experiments reasonably well. We note that, to obtain a more accurate match, further improvements are required, both to the slip velocities used in the model and the experimental datasets in the literature.

Appendix B. Particle tracking - simulations

To get comparable bubble growth data from simulations, the particle tracing feature in COMSOL was employed. 72 massless tracer particles were released from the electrode every 0.5 mm along the electrode height. The velocities of these particles are set to the gas velocity ($\mathbf{u_g}$) obtained from the solved flowfield. The diameters of each of the particles are then obtained by interpolating the values of the diameter distribution, obtained from the solved flowfield, to the trajectory of the particle. The trajectories chosen for the comparison in the main validation presented in Fig. 5 correspond to the extremities of the release locations of the tracked bubbles from experiments. All the pathlines of the particle tracing simulations for a gas-evolution efficiency of $f_g = 0.4$ are shown in Fig. B.1.

Data availability

Data will be made available on request.

References

[1] IEA, Global Hydrogen Review 2024, Technical Report, IEA, 2024.
[2] N.S. Hassan, A.A. Jalil, S. Rajendran, N.F. Khusnun, M.B. Bahari, A. Johari, M.J. Kamaruddin, M. Ismail, Recent review and evaluation of green hydrogen production via water electrolysis for a sustainable and clean energy society, Int. J. Hydrog. Energy 52 (2024) 420–441.
[3] Yujing Guo, Gendi Li, Junbo Zhou, Yong Liu, Comparison between hydrogen production by alkaline water electrolysis and hydrogen production by PEM electrolysis, IOP Conf. Ser.: Earth Environ. Sci. 371 (4) (2019) 042022.
[4] Shigeo Shibata, The concentration of molecular hydrogen on the platinum cathode, Bull. Chem. Soc. Japan 36 (1) (1963) 53–57.
[5] S. Shibata, Supersaturation of oxygen in acidic solution in the vicinity of an oxygen-evolving platinum anode, Electrochim. Acta 23 (7) (1978) 619–623.
[6] N. Nagai, M. Takeuchi, T. Kimura, T. Oka, Existence of optimum space between electrodes on hydrogen production by water electrolysis, Int. J. Hydrog. Energy 28 (1) (2003) 35–41.
[7] John Eigeldinger, Helmut Vogt, The bubble coverage of gas-evolving electrodes in a flowing electrolyte, Electrochim. Acta 45 (27) (2000) 4449–4456.
[8] J.W. Haverkort, H. Rajaei, Voltage losses in zero-gap alkaline water electrolysis, J. Power Sources 497 (2021) 229864.
[9] Rainier Hreiz, Lokmane Abdelouahed, Denis Fuenfschilling, Francois Lapicque, Electrogenerated bubbles induced convection in narrow vertical cells: PIV measurements and Euler–Lagrange CFD simulation, Chem. Eng. Sci. 134 (2015) 138–152.
[10] Willem Haverkort, Electrolysers, Fuel Cells and Batteries: Analytical Modelling, TU Delft OPEN Publishing, 2024, p. 168.
[11] J.W. Haverkort, A general mass transfer equation for gas-evolving electrodes, Int. J. Hydrog. Energy 74 (2024) 283–296.
[12] N. Valle, J.W. Haverkort, Self-similar solution for laminar bubbly flow evolving from a vertical plate, J. Fluid Mech. 996 (2024) A38.
[13] N. Valle, J.W. Haverkort, Analytical mass transfer coefficients for natural convection from vertical gas-evolving electrodes, Int. J. Heat Mass Transfer 225 (2024) 125390.
[14] Jonathan Schillings, Olivier Doche, Jonathan Deseure, Modeling of electrochemically generated bubbly flow under buoyancy-driven and forced convection, Int. J. Heat Mass Transfer 85 (2015) 292–299.
[15] Anders A. Dahlkild, Modelling the two-phase flow and current distribution along a vertical gas-evolving electrode, J. Fluid Mech. 428 (2001) 249–272.
[16] Patrick Boissonneau, Philip Byrne, An experimental investigation of bubble-induced free convection in a small electrochemical cell, J. Appl. Electrochem. 30 (7) (2000) 767–775.
[17] Daniel Lumanauw, Hydrogen Bubble Characterization in Alkaline Water Electrolysis (Mster thesis), University of Toronto, 2000.
[18] Lokmane Abdelouahed, Rainier Hreiz, Souhila Poncin, Gérard Valentin, Francois Lapicque, Hydrodynamics of gas bubbles in the gap of lantern blade electrodes without forced flow of electrolyte: Experiments and CFD modelling, Chem. Eng. Sci. 111 (2014) 255–265.
[19] Vincent S.J. Craig, Barry W. Ninham, Richard M. Pashley, The effect of electrolytes on bubble coalescence in water, J. Phys. Chem. 97 (39) (1993) 10192–10197.
[20] Timothy T. Duignan, The surface potential explains ion specific bubble coalescence inhibition, J. Colloid Interface Sci. 600 (2021) 338–343.
[21] Pierre Van De Velde, Benoit Scheid, Joris Proost, Benoît Haut, Induced flow and coalescence effects on hydrogen bubble size distribution around a single wire electrode in alkaline water electrolysis.+, Chem. Eng. Sci. (2025) 121598.
[22] A. Zarghami, N.G. Deen, A.W. Vreman, CFD modeling of multiphase flow in an alkaline water electrolyzer, Chem. Eng. Sci. 227 (2020) 115926.
[23] H. Vogt, The rate of gas evolution at electrodes—II. An estimate of the efficiency of gas evolution on the basis of bubble growth data, Electrochim. Acta 29 (2) (1984) 175–180.
[24] H. Vogt, On the gas-evolution efficiency of electrodes I–theoretical, Electrochim. Acta 56 (3) (2011) 1409–1416.
[25] H. Vogt, On the gas-evolution efficiency of electrodes. II–numerical analysis, Electrochim. Acta 56 (5) (2011) 2404–2410.
[26] H. Vogt, Heat transfer in boiling and mass transfer in gas evolution at electrodes–The analogy and its limits, Int. J. Heat Mass Transfer 59 (2013) 191–197.
[27] Khalid Zouhri, Seong-young Lee, Evaluation and optimization of the alkaline water electrolysis ohmic polarization: exergy study, Int. J. Hydrog. Energy 41 (18) (2016) 7253–7263.
[28] Aviral Rajora, Johannes Wilhelmus Haverkort, An analytical multiphase model for membraneless alkaline water electrolyzers, in: Electrochemical Society Meeting Abstracts 240, no. 1, The Electrochemical Society, Inc., 2021, p. 178.
[29] Damien Le Bideau, Philippe Mandin, Mohamed Benbouzid, Myeongsub Kim, Mathieu Sellier, Fabrizio Ganci, Rosalinda Inguanta, Eulerian two-fluid model of alkaline water electrolysis for hydrogen production, Energies 13 (2020).
[30] Steffen Hess, Shidong Zhang, Thomas Kadyk, Werner Lehnert, Michael Eikerling, Steven B. Beale, Numerical two-phase simulations of alkaline water electrolyzers, ECS Trans. 112 (4) (2023) 419.
[31] Xudong Duan, Aimin Zhou, Qiaomai Liu, Juan Xiao, Jian Wen, Simin Wang, Numerical simulation and structural optimization of electrolyzer based on the coupled model of electrochemical and multiphase flow, Int. J. Hydrog. Energy 49 (2024) 604–615.
[32] Koji Matsuura, Yoko Yamanishi, Chao Guan, Shinichiro Yanase, Control of hydrogen bubble plume during electrolysis of water, J. Phys. Commun. 3 (3) (2019) 035012.
[33] Kota Ando, Yoshiharu Uchimoto, Takashi Nakajima, Concentration profile of dissolved gas during hydrogen gas evolution: an optical approach, Chem. Commun. 56 (92) (2020) 14483–14486.
[34] Prasad Chandran, Shamit Bakshi, Dhiman Chatterjee, Study on the characteristics of hydrogen bubble formation and its transport during electrolysis of water, Chem. Eng. Sci. 138 (2015) 99–109.
[35] Kurian J. Vachaparambil, Kristian Etienne Einarsrud, Numerical simulation of bubble growth in a supersaturated solution, Appl. Math. Model. 81 (2020) 690–710.
[36] Kurian J. Vachaparambil, Kristian Etienne Einarsrud, Numerical simulation of continuum scale electrochemical hydrogen bubble evolution, Appl. Math. Model. 98 (2021) 343–377.
[37] Hongbo Liu, Liang-ming Pan, Jian Wen, Numerical simulation of hydrogen bubble growth at an electrode surface, Can. J. Chem. Eng. 94 (1) (2016) 192–199.
[38] Pablo Peñas, Peter van der Linde, Wouter Vijselaar, Devaraj van der Meer, Detlef Lohse, Jurriaan Huskens, Han Gardeniers, Miguel A. Modestino, David Fernandez Rivas, Decoupling gas evolution from water-splitting electrodes, J. Electrochem. Soc. 166 (15) (2019) H769.
[39] F. Khalighi, A.W. Vreman, Y. Tang, N.G. Deen, Effects of the boundary conditions at the gas-liquid interface on single hydrogen bubble growth in alkaline water electrolysis, Chem. Eng. Sci. 301 (2025) 120666.
[40] Akash Raman, Carla Corina dos Santos Porto, Han Gardeniers, Cíntia Soares, David Fernández Rivas, Natan Padoin, Investigating mass transfer around spatially-decoupled electrolytic bubbles, Chem. Eng. J. 477 (2023) 147012.
[41] Gerd Mutschke, D. Baczyzmalski, C. Cierpka, F. Karnbach, M. Uhlemann, X. Yang, K. Eckert, J. Fröhlich, Numerical simulation of mass transfer and convection near a hydrogen bubble during water electrolysis in a magnetic field, Magnetohydrodynamics 531 (2017) 193–199.
[42] Hanan Mohamed Mohsin, Yuting Zhuo, Yansong Shen, Eulerian-Eulerian-VOF multifluid modelling of liquid–gas reacting flow for hydrogen generation in an alkaline water electrolyser, Fuel 373 (2024) 132164.
[43] Jaeseung Lee, Afroz Alam, Chungi Park, Soobin Yoon, Hyunchul Ju, Modeling of gas evolution processes in porous electrodes of zero-gap alkaline water electrolysis cells, Fuel 315 (2022) 123273.
[44] J.A. Almonacid, A.K. Aydin, J.A. Roberts, M.D. Shirley, Bubbles in flow streams and porous media, Math. Ind. Rep. (MIIR) (2023).
[45] Yikai Chen, Nathan S. Lewis, Numerical simulation and modeling of hydrogen gas evolution on planar and microwire array electrodes, J. Electrochem. Soc. 169 (6) (2022) 066510.
[46] J.W. Haverkort, H. Rajaei, Electro-osmotic flow and the limiting current in alkaline water electrolysis, J. Power Sources Adv. 6 (2020) 100034.
[47] P. Trinke, P. Haug, J. Brauns, B. Bensmann, R. Hanke-Rauschenbach, T. Turek, Hydrogen crossover in PEM and alkaline water electrolysis: mechanisms, direct comparison and mitigation strategies, J. Electrochem. Soc. 165 (7) (2018) F502.
[48] Philipp Haug, Matthias Koj, Thomas Turek, Influence of process conditions on gas purity in alkaline water electrolysis, Int. J. Hydrog. Energy 42 (15) (2017) 9406–9418.
[49] Matheus T. de Groot, Joost Kraakman, Rodrigo Lira Garcia Barros, Optimal operating parameters for advanced alkaline water electrolysis, Int. J. Hydrog. Energy 47 (82) (2022) 34773–34783.
[50] Mamoru Ishii, Takashi Hibiki, Thermofluid Dynamics of Two-Phase Flow, Springer, 2011.
[51] COMSOL, CFD module user's guide, 2023.
[52] JF t RICHARDSON, Sedimentation and fluidisation: Part I, Trans. Inst. Chem. Eng. 32 (1954) 35–53.
[53] H. Nicolai, B. Herzhaft, E.J. Hinch, L. Oger, E. Guazzelli, Particle velocity fluctuations and hydrodynamic self-diffusion of sedimenting non-Brownian spheres, Phys. Fluids 7 (1) (1995) 12–23.
[54] J.M. Ham, G.M. Homsy, Hindered settling and hydrodynamic dispersion in quiescent sedimenting suspensions, Int. J. Multiph. Flow 14 (5) (1988) 533–546.
[55] Shusaku Harada, Ryoko Otomo, Diffusive behavior of a thin particle layer in fluid by hydrodynamic interaction, Phys. Rev. E 80 (6) (2009) 066311.
[56] A. Rajora, J.W. Haverkort, An analytical multiphase flow model for parallel plate electrolyzers, Chem. Eng. Sci. 260 (2022) 117823.
[57] A. Rajora, J.W. Haverkort, An analytical model for the velocity and gas fraction profiles near gas-evolving electrodes, Int. J. Hydrog. Energy 48 (71) (2023) 27450–27463.
[58] W.L. van der Does, N. Valle, J.W. Haverkort, Multiphase alkaline water electrolysis simulations: the need for a solid pressure model to explain experimental bubble overpotentials, Int. J. Hydrog. Energy tbd (2025) tbd.
[59] P.G.T. Saffman, The lift on a small sphere in a slow shear flow, J. Fluid Mech. 22 (2) (1965) 385–400.

[60] John B. McLaughlin, Inertial migration of a small sphere in linear shear flows, J. Fluid Mech. 224 (1991) 261–274.
[61] Renwei Mei, An approximate expression for the shear lift force on a spherical particle at finite Reynolds number, Int. J. Multiph. Flow 18 (1) (1992) 145–147.
[62] David Leighton, Andreas Acrivos, The shear-induced migration of particles in concentrated suspensions, J. Fluid Mech. 181 (1987) 415–439.
[63] Roland Clift, John R. Grace, Martin E. Weber, Bubbles, Drops, and Particles, Courier Corporation, 2005.
[64] R. Byron Bird, Warren E. Stewart, Edwin N. Lightfoot, Transport Phenomena, Revised 2nd Edition, John Wiley & Sons, Inc New York, 2006.
[65] Wei Xing, Min Yin, Qing Lv, Yang Hu, Changpeng Liu, Jiujun Zhang, Oxygen solubility, diffusion coefficient, and solution viscosity, in: Rotating Electrode Methods and Oxygen Reduction Electrocatalysts, Elsevier, 2014, pp. 1–31.
[66] Caroline A. Schneider, Wayne S. Rasband, Kevin W. Eliceiri, NIH Image to ImageJ: 25 years of image analysis, Nature Methods 9 (7) (2012) 671–675.
[67] P.J. Roache, Perspective: A method for uniform reporting of grid refinement studies, J. Fluids Eng. 116 (3) (1994) 405–413.
[68] Lokmane Abdelouahed, Gérard Valentin, Souhila Poncin, François Lapicque, Current density distribution and gas volume fraction in the gap of lantern blade electrodes, Chem. Eng. Res. Des. 92 (3) (2014) 559–570.